Supplementary Materials:

Deterministic Model of Earthquake Clustering Shows Reduced Stress Drops for Nearby Aftershocks

Bruce E. Shaw[1*] , Keith Richards-Dinger[2] and James H. Dieterich[2]

[1]Lamont Doherty Earth Observatory, Columbia University

[2]Department of Earth Sciences, UC Riverside

[*]To whom correspondence should be addressed

Supplementary Materials

The Model

Our new physical model is based on a generalization of an extremely efficient quasistatic boundary element model developed by *Dieterich and Richards-Dinger* [2010]. The original model uses three key approximations. First, elements interact with quasistatic elastic interactions, so dynamic stresses are neglected. Second, rate-and-state frictional behavior is simplified into a three regime system where elements are either stuck, nucleating, or sliding dynamically. Third, during dynamic sliding slip-rate is fixed at a constant sliding rate. These approximations allow for analytic treatments of rate and state behaviors in different sliding regimes, and a tremendous speed-up computationally over inertial [*Bouchon and Streiff*, 1997; *Andrews*, 1999; *Harris and Day*, 1999; *Aagaard et al.*, 2004; *Day et al.*, 2005; *Dalguer and Day*, 2007; *Harris et al.*, 2009; *Lapusta and Liu*, 2009] and traditional quasistatic methods [*Ben-Zion and Rice*, 1997; *Ward*, 2000]. A discussion of parameters and their sensitivities in the model is presented at the end of the supplement.

While the simulations were developed and run on modest clusters, to get enough spatial resolution to compare spatial distributions of events with observations at smaller magnitudes, we need to turn to supercomputers. Figures 3-5 in the main text shows results of an analysis of a simulation on a supercomputer with grid resolution of $.28km$ sided triangles for a six stranded 150 km long fault zone (run on NSF's TACC Stampede supercomputer. This run was done on 2048 processors in a 5 hour run).

Geometrical incompatibilities and long term slip

Backslip is a standard way of dealing with geometrical incompatibilities leading to accumulating stresses. There, slips are proscribed as having long-term rates, and heterogeneous stressing rates that produce those long term rates are calculated and then imposed as loading conditions. This works, but at the cost of needing to know what slip rates to impose, and some inherent smoothing of the underlying geometry. Plastic deformation off of the fault is another widely used technique for dealing with accumulating stresses [*Rudnicki and Rice*, 1975; *Andrews*, 2005; *Ben-Zion and Shi*, 2005; *Duan and Day*, 2008; *Ma and Beroza*, 2008; *Templeton and Rice*, 2008; *Viesca et al.*, 2008; *Dunham et al.*, 2011b]. This is an appealing, self consistent approach, though is itself a likely approximation of more localized secondary structures, as faults are more generally seen in the field as consisting of multiple surfaces. We have a few ways of dealing with geometrical incompatibility issues in our model. One using multiple strands significantly extends the regime of system level geometrical compatibility, so much larger strains can be accommodated elastically. Secondly, while our boundary elements are not suited to bulk plastic deformation, we can also employ an approximate stress limiting process on the faults, putting floors and ceilings on stress components on the boundary fault elements. This optional feature adds a way of approximately mimicking unmodeled off fault stress limiting processes. A parameter f_σ putting a floor on normal stress which is a fraction multiplying the initial normal stress is one way of doing this which has been applied and appears useful.

Additional figures showing further model details and results.

The rough fault geometry we examine is based on a band limited self similar geometry [*Dunham et al.*, 2011a; *Fang and Dunham*, 2013; *Sahimi*, 1998]. Constructed from an inverse fourier transform of a controlled spectral density of fourier transformed noise, it allows for controlled short and long wavelength cutoffs. We take advantage of the capability of the RSQSim infrastructure to efficiently simulate triangular elements [*Gimbutas et al.*, 2012], which allows a continuous covering of the rough surface.

By downsampling more resolved rough representations, we can also explore different grid resolutions of the same underlying specific roughness case. Figure S-1 illustrates this looking at the slip on a single rough fault, with changed downsample coarseness. Note the effect of the back slip stress reducing slip on the more resolved faults [*Dieterich and Smith*, 2009; *Dunham et al.*, 2011a; *Fang and Dunham*, 2013].

Connecting individual strands into a fault system, we see interesting collective effects. To link into a multistranded fault, we connect all the faults at the two surface end points by subtracting off a linear trend for each strand. Figure S-2 illustrates the result of looking at the same grid resolution, but changing the small-scale roughness cutoff in the spectral density. Here, we drop modes above changing cutoffs, zeroing the amplitudes of a cutoff wave number scale. Interestingly, collectively the system behaves similarly in terms of the overall deformation. But locally, there are significant rearrangements in how the system partitions deformation across the various strands, as limiting back stresses at changing smallest scales leads to alternative pathways for system level deformation. Thus, we see interesting behaviors related to deformation on individual faults and across a system of faults, in a well controlled setting.

Distribution of sizes of events

Figure S-3 shows the distribution of sizes of events. We see a power law distribution of small events along with a characteristic distribution of large events which occur above the extrapolated small event rate. There is some sensitivity in the distribution of sizes of events to the rupture parameter a, with larger a giving a steeper slope in the power law of small events. The minimum magnitude is also set by the grid resolution parameters δ_x and δ_z, which also have some weak impact on the slope of the small events. The rolloff in the distribution of sizes below M3 illustrates the minimum magnitude of events at this resolution in the model.

Criteria for Mainshock and Aftershock Selection

As discussed in the main text, we use a fixed time and space window, and count as mainshocks only events with a preceding and following window in space and time with no larger events. Other types of algorithms have been developed for separating mainshocks, foreshocks, and aftershocks based on most probably-causal space-time connections [*Baiesi and Paczuski*, 2004; *Bottiglieri et al.*, 2009; *Zaliapin et al.*, 2008]. The causal algorithms offer a more complete way of disentangling the population. But since incompleteness in the classification is not an issue for us, nor is precise parentage, but unambiguousness is, we operate in a conservative region of that broader causal space, finding the simplicity of conservative space-time windows useful.

Default numerical values for the windowing parameters we use are as follows. $T_{before} = 500$ days $T_{after} = 30$ days $R_{max} = 40$ km, with no event larger than the mainshock occurring in the time period preceding and following the mainshock over the lengthscale R_{max}

Productivity

In addition to the spatial and temporal features of the aftershocks, the overall rates of aftershocks, the productivity as a function of mainshock magnitude, is another quantity we would like to get right in the models. That is, we could get the spatial distributions right, but be way off in the rates of events. Figure S-4 suggests we may be doing pretty well, however. Figure S-4 shows a comparison with Bath's law, which states that on average the largest aftershock is around 1.2 magnitude units smaller than the mainshock (with aftershocks restricted to have magnitudes smaller than the mainshock). In the figure, the dotted line shows Bath's law, compared with the model results. As noted in the main text, the aftershock and foreshock productivity does have some sensitivity to the logarithmic strengthening friction a parameter, but for appropriately chosen parameter ranges we do find consistency with Bath's law.

Stress drop estimates from macroscopic information

Even when we don't have privileged information, we can see from magnitude area scaling the lower stress drops. Figure S-5 illustrates this by using macroscopic information, magnitude and source area, to estimate stress drops. As with directly measured information we see, on average, lower stress drops for nearby aftershocks.

Rebreaking of mainshock rupture area

We can use privileged information about what broke in the mainshock to explore further the question of rebreaking incompletely healed fault surface leading to low stress drops. Figure S-6 shows this from two points of view. Figure S-6a shows, for nearby aftershocks, the fraction of the mainshock rupture area which is being rebroken for different magnitude aftershocks, with points color coded by the friction drop in the event. We see a clear trend that events which have a substantial fraction of their rupture area having rebroken areas which broke in the mainshock have lower friction drops, evidenced by the colder colors occurring at larger fractions. We also see some magnitude dependence in the model to the friction drops, with larger magnitudes having systematically lower friction drops. This is not an appealing feature of the model, given observations which suggest earthquake stress drops appear to be independent of magnitude [*Hanks*, 1977; *Shaw*, 2013], but it does not obviate the relative stress drop effects we see at a given magnitude for nearby aftershocks relative to similar magnitude mainshocks. Figure S-6b shows the friction drop for nearby aftershocks of given magnitude as a function of hypocentral distance from the nearest part of the mainshock rupture. This is shown on a log distance scale, with points again color coded by friction drop. There is substantial scatter in the effect, but we do see lower friction drops tending to occur on the events initiating closer to the mainshock rupture area. This is evidenced by warmer colors tending to lie above the cooler colors at a given magnitude.

Parameters in Model

For completeness, we reproduce in the Table all the parameters in the model. The rupture parameters are discussed in more detail in [*Dieterich and Richards-Dinger*, 2010; *Richards-Dinger and Dieterich*, 2012]. There is very little sensitivity to the results to the vast majority of the parameters. Where changing the parameters by a factor of 2 either up or down makes little difference, we have labeled the sensitivity as being not sensitive. Only one parameter, the logarithmic strengthening friction parameter a was found to have sensitivity in the results.

Table 1: Model Parameters

(a) Rupture Parameters

Param	Value	Physical Significance	Sensitivity and Impacts
a	.00025	ln velocity strengthening	Sensitive; Increasing gives more aftershocks
b	.005	state velocity weakening	not sensitive as long as $b > a$
$b - a$	.00475	stress drop	not sensitive; sets stress drop scale
μ_0	.6	constant friction coeff	not sensitive
D_c	1e-6 m	friction weakening distance	not sensitive
σ	100 Mpa	initial normal stress	not sensitive; sets stress drop scale
f_τ	.1	dynamic stress overshoot	not sensitive; mimics inertial overshoot
f_σ	.5	limits reduction in σ	not sensitive; plastic term allowing long simulations
V_s	1 m/s	dynamic slip rate	not sensitive; sets dynamic sliding velocity

(b) Fault Geometry Parameters

Param	Value	Physical Significance	Sensitivity and Impacts
α	.03	roughness	increasing gives more aftershocks
L	150 km	fault length	not sensitive as long as $L \gg W$
W	12 km	fault downdip width	not sensitive; affects maximum slip
L_0	1 km	small lenghtscale roughness	not sensitive
L_c	50 km	large lenghtscale roughness	not sensitive; limits fault zone width
N	6	number of strands	not sensitive; increasing gives more productivity
δ_x	.2 km	grid res. along-strike	not sensitive; affects distribution of sizes
δ_z	.2 km	grid res. down-dip	not sensitive; affects distribution of sizes
$\dot{\nu}$	1e-10	loading strain rate	not sensitive; sets event rate
λ	30 GPa	Lame' lambda elastic coeff	not sensitive
μ	30 GPa	Lame' mu elastic coeff	not sensitive

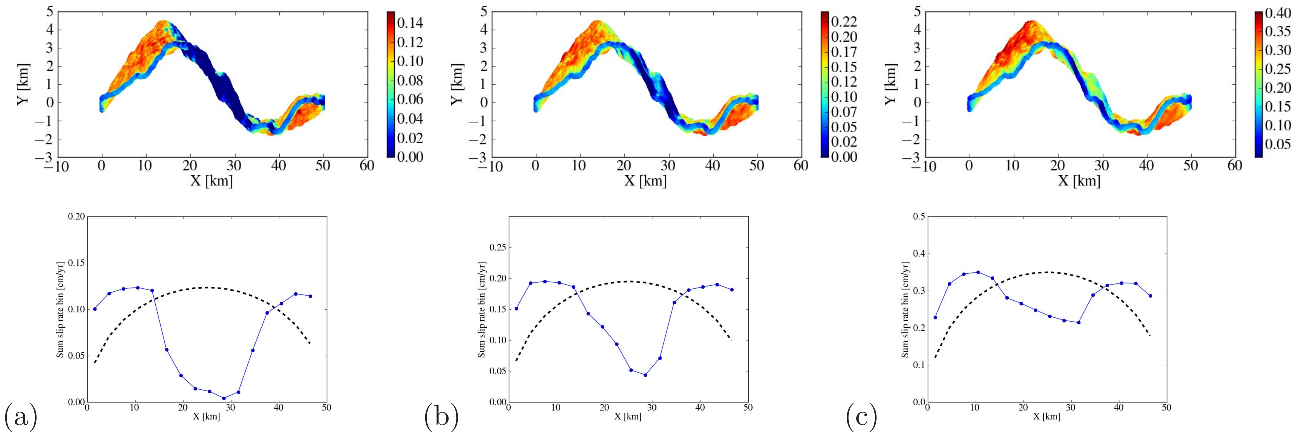

Figure S-1: Rough single strand at changing downsampled spatial resolution. Top figures show slip on faults, bottom summed slip. (a) Most resolved [60m triangular elements]. (b) Factor of 2 less. (c) Factor of 4 less. Note slip increasing and becoming more crack-like on the smoother faults.

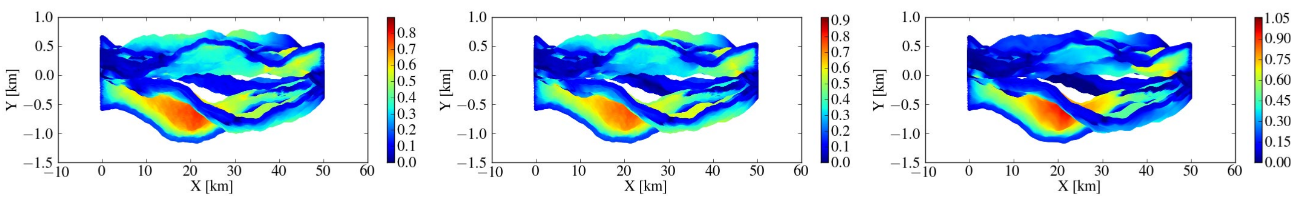

Figure S-2: Rough single strand at changing small wavelength cutoff L_0. Grid resolution here is $.16km$ triangular elements. (a) $L_0 = .25km$ (b) $L_0 = .62km$ (c) $L_0 = .82km$ Note slip increasing and becoming more concentrated on the smoother faults. Not also that slip partitioning between faults depends on small scale features.

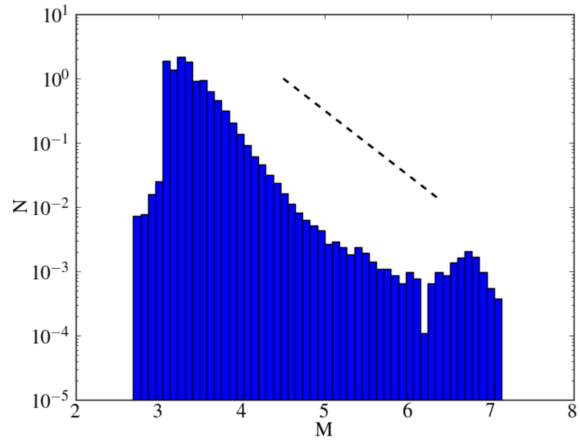

Figure S-3: Distribution of sizes of events. Note power law distribution of small event magnitudes and characteristic distribution excess of large events above the extrapolated small event rate. Dashed line shows $b = 1$ slope for comparison.

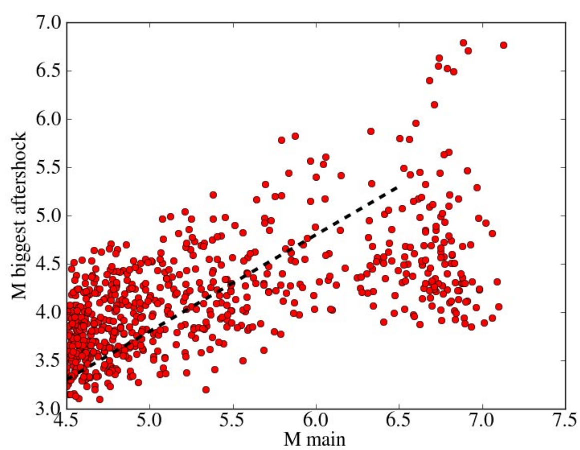

Figure S-4: Bath's law compared with model data. Magnitude of the largest aftershock on the vertical axis versus mainshock magnitude on the horizontal axis. Dashed line shows Bath's law, that the magnitude difference is on average 1.2 magnitude units.

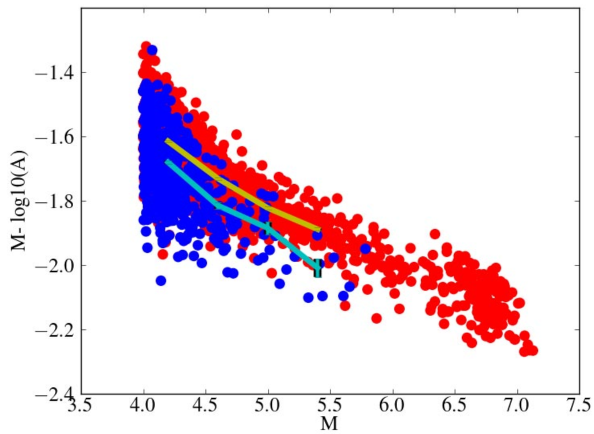

Figure S-5: Lower median stress drops for aftershocks relative to mainshocks in model. Inferred stress drop from magnitude and source area. Vertical axis shows magnitude minus log_{10} Area, which scales as static stress drop for circular ruptures. Horizontal axis is Magnitude. Red circles are individual mainshocks, blue circles are individual nearby aftershocks. The blue circles tending to lie below the red circles at a given magnitude illustrates the differences in the statistics of the populations. Solid lines show averages for a given magnitude of the two populations, with yellow showing mainshocks and cyan showing nearby aftershocks. Systematic lowering is shown by cyan curve lying below yellow curve. Error bars on curves show one standard error uncertainty in mean.

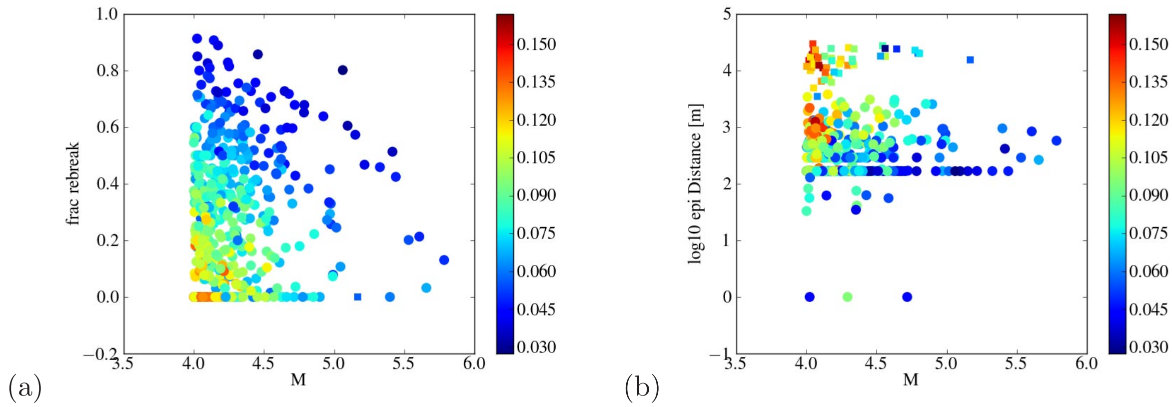

Figure S-6: (a) Fraction of aftershock area rebreaking mainshock area. Horizontal axis is magnitude of the aftershock; vertical axis is fraction of aftershock area having broken in mainshock. Color shows mean friction drop in aftershock. Warmer colors slying above cooler colors shows higher fraction rebreaking having lower stress drops. Only aftershocks above a cutoff magnitude of M4 are shown. (b) Friction drop of nearby aftershocks as a function of distance of aftershock hypocenter from closest part of mainshock rupture area. Horizontal axis is magnitude of the aftershock; vertical axis is $\log_{10}$ of distance in meters (aftershock hypocenters which broke previously in mainshock are given minimal cutoff distance of 1m; they are rare, but do exist). Color shows mean friction drop in aftershock.

References

Aagaard, B. T., G. Anderson, and K. W. Hudnut, Dynamic rupture modeling of the transition from thrust to strike-slip motion in the 2002 Denali Fault earthquake, Alaska, *Bull. Seismol. Soc. Am.*, *94*, S190, 2004.

Andrews, D., Rupture dynamics with energy loss outside the slip zone, *J. Geophys. Res.*, *110*, 2005.

Andrews, D. J., Test of two methods for faulting in finite-difference calculations, *Bull. Seismol. Soc. Am.*, *89*, 931, 1999.

Baiesi, M., and M. Paczuski, Scale-free networks of earthquakes and aftershocks, *Phys. Rev. E*, *69*, 2004.

Ben-Zion, Y., and J. R. Rice, Dynamic simulations of slip on a smooth fault in an elastic solid, *J. Geophys. Res.*, *102*, 17,771, 1997.

Ben-Zion, Y., and Z. Shi, Dynamic rupture on a material interface with spontaneous generation of plastic strain in the bulk, *Earth Plan. Sci. Lett.*, *236*, 486–496, 2005.

Bottiglieri, M., E. Lippiello, C. Godano, and L. de Arcangelis, Identification and spatiotemporal organization of aftershocks, *J. Geophys. Res.*, *114*, 2009.

Bouchon, M., and D. Streiff, Propagation of a shear crack on a nonplanar fault: a method of calculation, *Bull. Seismol. Soc. Am.*, *87*, 61, 1997.

Dalguer, L. A., and S. M. Day, Staggered-grid split-node method for spontaneous rupture simulation, *J. Geophys. Res.*, *112*, B02,302, 2007.

Day, S. M., L. A. Dalguer, N. Lapusta, and Y. Liu, Comparison of finite difference and boundary integral solutions to three-dimensional spontaneous rupture, *J. Geophys. Res.*, *110*, B12,307, 2005.

Dieterich, J. H., and K. B. Richards-Dinger, Earthquake recurrence in simulated fault systems, *Pageoph*, *167*, 1087, 2010.

Dieterich, J. H., and D. E. Smith, Nonplanar Faults: Mechanics of Slip and Off-fault Damage, *Pageoph*, *166*, 1799, 2009.

Duan, B., and S. M. Day, Inelastic strain distribution and seismic radiation from rupture of a fault kink, *J. Geophys. Res.*, *113*, 2008.

Dunham, E. M., D. Belanger, L. Cong, and J. E. Kozdon, Earthquake Ruptures with Strongly Rate-Weakening Friction and Off-Fault Plasticity, Part 2: Nonplanar Faults, *Bull. Seismol. Soc. Am.*, *101*, 2308, 2011a.

Dunham, E. M., D. Belanger, L. Cong, and J. E. Kozdon, Earthquake Ruptures with Strongly Rate-Weakening Friction and Off-Fault Plasticity, Part 1: Planar Faults, *Bull. Seismol. Soc. Am.*, *101*, 2296–2307, 2011b.

Fang, Z., and E. M. Dunham, Additional shear resistance from fault roughness and stress levels on geometrically complex faults, *J. Geophys. Res.*, *118*, 3642–3654, 2013.

Gimbutas, Z., L. Greengard, M. Barall, and T. E. Tullis, On the Calculation of Displacement, Stress, and Strain Induced by Triangular Dislocations, *Bull. Seismol. Soc. Am.*, *102*, 2776–2780, 2012.

Hanks, T. C., Earthquake stress-drops, ambient tectonic stresses, and the stresses that drive plates, *Pure Appl. Geophys.*, *115*, 441–458, 1977.

Harris, R. A., and S. M. Day, Dynamic 3D simulations of earthquake on en echelon fault, *Geophys. Res. Lett.*, *26*, 2089, 1999.

Harris, R. A., et al., The SCEC/USGS dynamic earthquake rupture code verification exercise, *Seismol. Res. Lett.*, *80*, 119, 2009.

Lapusta, N., and Y. Liu, Three-dimensional boundary integral modeling of spontaneous earthquake sequences and aseismic slip, *J. Geophys. Res.*, *114*, 2009.

Ma, S., and G. C. Beroza, Rupture dynamics on a bimaterial interface for dipping faults, *Bull. Seismol. Soc. Am.*, *98*, 1642–1658, 2008.

Richards-Dinger, K., and J. H. Dieterich, RSQSim Earthquake Simulator, *Seismol. Res. Lett.*, *83*, 983, 2012.

Rudnicki, J., and J. Rice, Conditions for localization of deformation in pressure-sensitive dilatant materials, *J. Mech. Phys. Sol.*, *23*, 371–394, 1975.

Sahimi, M., Non-linear and non-local transport processes in heterogeneous media: from long-range correlated percolation to fracture and materials breakdown, *Physics Reports*, *306*, 213, 1998.

Shaw, B. E., Earthquake surface slip length data is fit by constant stress drop and is useful for seismic hazard analysis, *Bull. Seismol. Soc. Am.*, *103*, 876, 2013.

Templeton, E. L., and J. R. Rice, Off-fault plasticity and earthquake rupture dynamics: 1. Dry materials or neglect of fluid pressure changes, *J. Geophys. Res.*, *113*, 2008.

Viesca, R. C., E. L. Templeton, and J. R. Rice, Off-fault plasticity and earthquake rupture dynamics: 2. Effects of fluid saturation, *J. Geophys. Res.*, *113*, 2008.

Ward, S., San Francisco Bay Area earthquake simulations: A step toward a standard physical earthquake model, *Bull. Seismol. Soc. Am.*, *90*, 370–386, 2000.

Zaliapin, I., A. Gabrielov, V. Keilis-Borok, and H. Wong, Clustering analysis of seismicity and aftershock identification, *Phys. Rev. Lett.*, *101*, 2008.